Carbon Monoxide and Formic Acid Oxidation at Rh@Pt Nanoparticles

Ehab N. El Sawy[a,b] *and Peter G. Pickup**[,a]

a. Department of Chemistry, Memorial University of Newfoundland, St. John's, NL, Canada, A1B 3X7
b. Department of Chemistry, School of Science and Engineering, American University in Cairo, AUC Avenue, P.O. Box 74, New Cairo 11835, Egypt

Electrochimica Acta 302 (2019) 234-240. https://doi.org/10.1016/j.electacta.2019.02.047

Abstract: Pt-based nanoparticle catalysts play a central role in the development of fuel cell technology. Due to their high susceptibility to poisoning by CO, the addition of a second metal is necessary to weaken its adsorption and/or increase its oxidation rate. In this work, we studied the effect of a rhodium core on CO and formic acid oxidation at core-shell nanoparticles synthesized by the sequential reduction of Rh and Pt using a polyol method. With increasing Pt coverage, the CO stripping potential was found to shift from 0.48 V vs. SCE for ca. 1 monolayer of Pt to 0.61 V for ca. 3 monolayers. The rapid shift with increasing Pt coverage is indicative of a strong electronic effect of the Rh core on the Pt shell. As a result of that strong electronic effect, the rate of the indirect oxidation of formic acid, via an adsorbed CO intermediate, was highest at low Pt coverages and gradually shifted towards that of Pt NPs with increasing Pt coverage. In contrast, the rate of the direct oxidation increased with increasing Pt coverage up to 2.3 monolayers and then decreased, suggesting that for low Pt coverages the advantage of weak CO adsorption was offset by the effects of weaker formic acid adsorption.

Keywords: carbon monoxide; formic acid; electrocatalysis; core-cell; nanoparticle; Rh@Pt

Corresponding Author

Peter G. Pickup: Tel: +709-864-8657. Fax: +709-864-3702. Email: ppickup@mun.ca

1. Introduction

Core-shell nanoparticles (NP) in which a metal core (M) is coated with one or more monolayers (ML) of Pt are becoming increasingly important in electrocatalysis [1-3]. Such M@Pt structures provide more efficient use of Pt and provide broad scope for controlling its electronic structure, geometric lattice strain, and surface reactivity. They have great potential in the development of catalysts for fuel cells. Fe, Co, Ni, and Cu cores have been widely employed in oxygen reduction catalysts [1, 3], while Pd [4-6], Au [4, 7, 8], Ru [9-12], and Rh [13-15] have been of most interest for the oxidation of alcohols and formic acid [2].

Rh@Pt catalysts, with a Pt shell over a Rh core, have been studied for CO [15, 16], formic acid [13], and ethanol [14, 15] oxidation. They have been shown to exhibit better activity than PtRh alloy NP for preferential oxidation of CO in H_2 [16], and shift the potential for electrochemical oxidation of adsorbed CO (CO_{ads}) to a lower potential relative to PtRh and Pt [15]. Weaker absorption of CO at Rh@Pt NP promotes the direct pathway for formic acid oxidation [13]. It was found that 2.6 ML of Pt on Rh nanocubes (ca. 7 nm) provided the highest activity. For ethanol oxidation, a catalyst prepared by deposition of Pt onto graphite supported Rh NP provided higher activities than Pt/C and it was inferred that there was more complete oxidation to CO_2 [14]. However, more well defined Rh@Pt NPs were found to be inferior to Ru@Pt for ethanol oxidation [15].

Insight into the role of the Rh core in controlling the activity of Rh@Pt NP for formic acid and ethanol oxidation has been provided by studies of the effects of the core on the electronic and geometric structure of the Pt shell. Lima and Gonzalez observed a shift in the Pt 5d band, due to charge transfer from the Pt shell to the Rh core, by X-Ray absorption spectroscopy (XANES) [15]. However, this effect was weaker than in PtRh alloy NP. The

lowering of the d-band center resulting from this charge transfer, attributed to both electronic and geometric (lattice compression) effects, would decrease the strength of CO adsorption. Harak et al. observed similar effects using X-ray photoelectron spectroscopy [13]. Rh@Pt with 1.2 ML of Pt showed the largest increase in the Pt 4f binding energy, while 7.4 ML exhibited the same binding energy as bulk Pt.

The changes in the Pt d-band center of M@Pt NP as the shell thickness is varied is due to electronic (ligand) effects, which occur over a few ML, and longer range geometric effects [17, 18]. Consequently, variation of the shell thickness provides control over the binding strength of CO and other adsorbates to the Pt surface, and there will be an optimal thickness for electrocatalysis of each reaction (e.g. oxidation of CO vs. formic acid vs. ethanol). Electrochemical oxidation of pre-adsorbed CO (CO stripping voltammetry) provides a measure of the combined electronic and geometric effects on the binding energy of the primary adsorbate and catalyst poison in the oxidation of organic fuels [19, 20]. This, in turn, provides a starting point for understanding their influence on the oxidation of fuels such as formic acid [21], methanol [10], and ethanol [15].

The purpose of the work reported here was to correlate the effects of the Pt shell thickness on the oxidation of CO and formic acid at Rh@Pt NP. Currently, CO stripping data for Rh@Pt NP is only available for a 1 ML shell [15], and formic acid oxidation has only been reported for nanocubes [13]. Since structures, electronic effects, geometric effects, and segregation of the Pt and Rh vary based on the synthesis method, shape, and size of the NP, it is crucial to compare CO and formic acid oxidation at the same Rh@Pt NP.

2. Experimental

2.1. Rh, Rh@Pt, and Pt NP synthesis

The Rh@Pt NP were prepared using a sequential procedure [11, 19, 20], in which the Rh core was synthesized first followed by the Pt shell. Rh NPs were synthesized using 0.1 mmol of $RhCl_3.3H_2O$ (Precious Metals Online) and 0.25 mmol of polyvinylpyrrolidone (PVP; Sigma-Aldrich; 40,000 g mol^{-1}) that were first dissolved in 20 ml of ethylene glycol (Sigma-Aldrich). The solution was gradually heated (5 °C min^{-1}) and maintained under reflux for 2 h. Pt shells, with various coverages, were deposited onto the Rh NP by the addition of K_2PtCl_4 (Fluka) in ethylene glycol (10 mL) and heating (5 °C min^{-1}) under N_2 at reflux for 2 h. Pt NPs were prepared similarly in ethylene glycol with PVP as the capping agent.

2.2. Characterization of Rh, Rh@Pt and Pt NP

Carbon supported catalyst samples, with 40 wt% Rh, Pt or Rh@Pt, were prepared for characterization and electrochemical experiments. The NPs were adsorbed onto Vulcan carbon (C; Cabot Corp.) by adding the colloidal NP solution to a homogenous mixture (by sonication) of C in ethanol. Following stirring for 4 h, acetone was added to facilitate the separation of the NP/C powder with a centrifuge. The Rh/C, Pt/C and Rh@Pt/C catalysts were washed well with acetone, and dried at 40-60 °C. Thermogravimetric analysis (TGA; TA Instruments Q500 TGA) in air/N_2 (1:1) was used to determine the metal loading on the carbon support. A Rigaku Ultima IV X-ray diffractometer (XRD) with CuK_α radiation was used to determine the NP crystal structure. The Rh:Pt ratios of the Rh@Pt/C samples were determined using energy-dispersive X-ray spectroscopy (EDS; JEOL JSM-7100F Field Emission Scanning Electron Microscope). A Tecnai Spirit scanning transmission electron microscope (STEM; The Electron Microscopy Unit

at Faculty of Medicine, Memorial University), was used to determine the sizes of the Rh and Rh@Pt NP.

2.3. Electrochemistry

Catalyst coated glassy carbon (GC) working electrodes (3 mm diameter) were prepared by suspending 1.5 mg of NP/C powder in 5 ml of water with sonication, applying 8.3 μl of the resulting "ink" onto the GC surface, and drying at ambient temperature. A glass cell with a saturated calomel electrode (SCE) and a Pt wire counter electrode in a separate compartment was used with a RDE4 potentiostat (Pine Instruments), operated by custom software. All solutions were prepared using Analar-grade chemicals and distilled, deionized water and purged with N_2. All measurements were made at ambient temperature (22 ± 1°C).

3. Results and discussion

3.1. Physical Characterization

Table 1 shows the targeted and measured atomic Rh:Pt ratios (x:y) of the core-shell particles. The measured ratio is used to identify each $Rh_x@Pt_y$ sample. For low Pt ratios, the compositions of the NP were close to the targeted values based on the amounts of $RhCl_3$ and K_2PtCl_4 employed, but the efficiency of Pt deposition decreased as the amount of K_2PtCl_4 was increased.

XRD patterns for the Rh, Rh@Pt, and Pt samples are shown in Fig. 1. They all show (111), (200), (220) and (311) peaks, at ca. 40°, 47°, 69° and 83°, respectively, with their position shifted from the Rh values towards Pt values as Pt was added to the Rh core. The (220) and (311) peaks for the Rh@Pt samples show distinct shoulders at lower angles, while the (111) and (200) peaks are slightly asymmetric but do not show clear shoulders in most cases. The shoulders and asymmetry become more pronounced with increasing Pt:Rh ratio.

Table 1. Target and measured (EDS) Rh:Pt atomic ratios, particles sizes, and estimated Pt coverages for carbon-supported Rh/C, Rh@Pt/C and Pt/C catalysts.

measured composition	target Rh:Pt atomic ratio	particle diameter (nm)			Pt monolayers (ML)
		XRD	calculated	TEM	
Rh		4.2		4.5±0.9	
$Rh_{72}@Pt_{28}$	71:29	4.4	4.7	4.0±1.4	0.9
$Rh_{60}@Pt_{40}$	59:41	4.5	5.0	5.3±2.1	1.4
$Rh_{54}@Pt_{46}$	50:50	4.7	5.2	4.6±1.9	1.8
$Rh_{46}@Pt_{54}$	40:60	4.8	5.4	5.5±1.8	2.3
$Rh_{40}@Pt_{60}$	34:66	4.9	5.7	5.6±1.9	2.7
Pt		3.3		4.1±0.7	

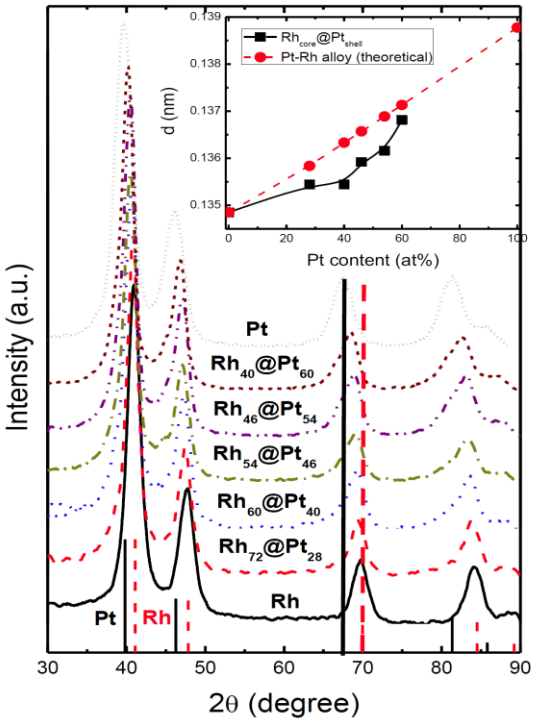

Figure 1. Powder XRD patterns of the Rh/C, Rh@Pt/C and Pt/C catalysts. The solid and dashed vertical lines represent the Rh FCC (PDF#05-0685) and Pt FCC (PDF#87-640) crystal phases, respectively. The inset shows the experimental (111) lattice spacing (■) and values for RhPt alloys estimated by Vegard's law (●).

Since Rh and Pt both have a fcc structure, the Pt shell will form part of the overall Rh@Pt unit cell, and there will be some compression of the Pt shell due to the lattice mismatch [13]. The shift to lower angle as the Pt content was increased can be attributed to a combination of the increasing contribution of the Pt shell and decreasing Pt lattice compression. The shoulders on some of the peaks and asymmetry of others indicates that there was some segregation of the Pt and Rh and is consistent with core@shell structures. The increases in the shoulders relative to the main peak as the Pt coverage was increased show the presence of a distinct Pt shell [13]. However, the thickness (size of the ordered domains) of the Pt shells is insufficient to resolve separate Pt peaks. A distinct Pt (200) peak has been reported for a 5.6 ML Pt shell on a 7 nm Rh cube [13], but the particle sizes and Pt coverages are too low here.

Further evidence for the formation of core@shell structures is provided by the composition dependence of the (111) lattice-spacing (d), shown in the inset of Fig. 1. Relative to the expected linear change from the Rh value to the Pt value (Vegard's law), the spacings for the Rh@Pt NP are lower, indicating that they are influenced by a distinct Rh core. As expected, this effect diminished as the Rh:Pt ratio was decreased until the spacing was close to that expected for an alloy at $Rh_{40}@Pt_{60}$. However, the asymmetry of the peaks for this composition shows that this coincidence is due expansion of the Rh core by the Pt shell, rather than the presence of an alloy phase.

Particle sizes, estimated from the widths of the (111) peaks in Fig. 1, are listed in Table1. The Rh particles used for the cores were estimated to be 4.2 nm in diameter, and this was supported by TEM (Fig. 2) which provided 4.5±0.9 nm. The TEM image shows that the Rh particles had a variety of shapes and that there was some aggregation.

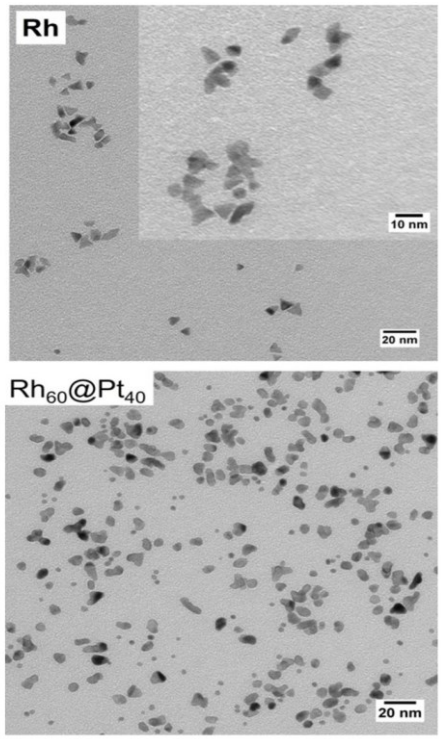

Figure 2. TEM images of the Rh and $Rh_{60}@Pt_{40}$ NP.

Based on the estimated Rh core size from XRD, and assuming a cuboctahedral geometry, estimates of particle sizes and the thicknesses of the Pt shells can be made for each Rh@Pt NP composition [16]. The calculated particle diameters ranged from ca. 4.7 to 5.7 nm, corresponding to Pt shell thicknesses in Pt monolayers (ML) ranging from ca. 0.9 to 2.7 ML (Table 1). The particle sizes observed by TEM (Fig. 2 and Table 1) are consistent with the calculated values, although there is considerable uncertainty due to the broad size distributions. In contrast, the average crystallite sizes obtained from XRD were somewhat smaller than the calculated sizes. This discrepancy can be attributed to the effects of the shoulders due to the Pt shell, which broadens the XRD peaks and causes underestimation of the crystallite size.

Although the XRD and TEM results provide compelling evidence that the Rh@Pt NP had core@shell structures, it is clear that each sample had a range of particle shapes and sizes.

Consequently, there would also have been a range of Pt coverages. If all of the particles in each sample had the same Rh:Pt ratio, then the smaller particles would have thinner Pt shells, because of their smaller volume to area ratio, and some would have had sub-monolayer coverages of Pt.

3.2. Electrochemical Characterization

Fig. 3 shows voltammograms of the Rh/C, Rh@Pt/C and Pt/C catalysts in 0.1 M H_2SO_4(aq). The upper potential limit was set at 0.8 V to minimize restructuring of the catalyst surface. Although this results in less than ideal voltammograms, it provides the best representation of the electrochemical characteristics of the as-prepared Rh@Pt NP. The voltammograms have been normalized by dividing by the sum of the millimoles of Rh and Pt atoms on each electrode in order to scale them relative to the Rh/C and Pt/C catalysts. They were stable over 5 cycles, but not tested over longer periods.

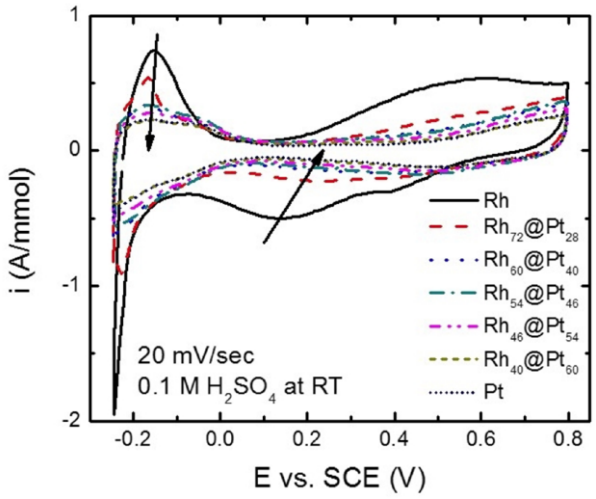

Figure 3. Cyclic voltammetry (20 mV s^{-1}) of Rh/C, Rh@Pt/C, and Pt/C coated GC electrodes in deaerated 0.1 M H_2SO_4.

The voltammetric profiles for all of the Rh@Pt NP are closer to the profile for Pt/C than Rh/C, as would be expected for core-shell structures. The voltammogram for the $Rh_{40}@Pt_{60}$/C

sample, which had on average 2.7 ML of Pt, is very similar to that for Pt/C, indicating that there was little influence of the Rh core on the surface of the Pt shell. This indicates that the Rh core had been completely covered and that the electronic and lattice compression effects of the Rh core were minor.

With decreasing Pt coverage, to 1.4 ML for $Rh_{60}@Pt_{40}/C$, the currents in the hydrogen adsorption/desorption region (-0.24 to ca. 0 V) increased slightly. However, for $Rh_{72}@Pt_{28}/C$ (0.9 ML), there was a large increase towards the values for Rh/C. There was a corresponding trend in the currents for oxide formation and reduction at potentials above 0 V, with the $Rh_{72}@Pt_{28}/C$ catalyst showing significant oxide formation and reduction at lower potentials than Pt/C and the other Rh@Pt/C catalysts. These changes with decreasing Pt coverage can be attributed to the growing electronic and strain effects of the Rh core [13]. The abrupt changes at ca. 1 ML can be attributed primarily to the electronic effect which would be most pronounced at 1 ML Pt coverage [10], and partial exposure of the Rh core. They indicate that the Pt coverages estimated from the Rh particle size and Rh:Pt ratio are reasonable.

3.3. Carbon Monoxide Stripping Voltammetry

Fig. 4 shows CO stripping voltammograms for the Rh/C, Rh@Pt/C and Pt/C catalysts. The currents have been divided by the peak current to emphasize differences in the peak position. It can be seen that CO oxidation occurred at a significantly lower potential (by 84 mV) at the Rh/C catalyst than at Pt/C. Addition of 0.9 ML of Pt to the Rh core ($Rh_{72}@Pt_{28}$) decreased the potential of the CO stripping peak by 47 mV. Increasing the thickness of the Pt shell resulted in a positive shift in the position of the CO stripping peak. At 1.4 ML ($Rh_{60}@Pt_{40}$), the shift relative to $Rh_{72}@Pt_{28}$ was only 27 mV and the peak was still at a lower potential than for Rh/C. However at 1.8 ML ($Rh_{54}@Pt_{46}$), the shift was 97 mV, and the peak was closer to that for Pt. At

2.7 ML ($Rh_{40}@Pt_{60}$), the position of the CO peak was not significantly different from that for Pt/C.

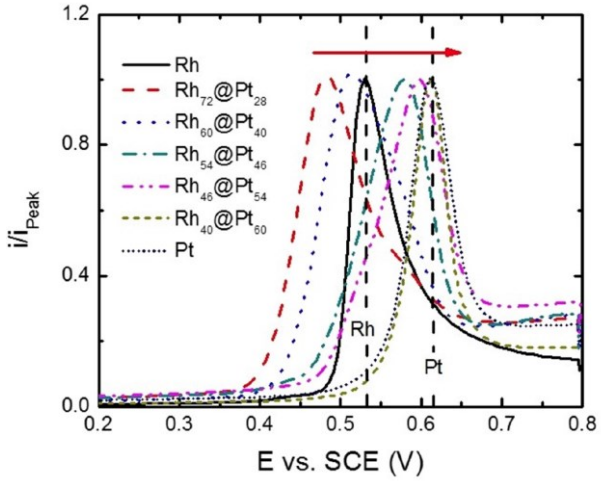

Figure 4. Stripping voltammetry (20 mV s^{-1}) in N_2 purged 0.1 M H_2SO_4 for CO adsorbed onto Rh/C, Rh@Pt/C, and Pt/C coated GC electrodes. CO was adsorbed from CO saturated 0.1 M H_2SO_4 for 15 min at -0.25 V. Currents have been normalized to the peak current to facilitate comparisons of peak positions and ratios.

Relative to Pt/C, the shift of -131 mV for 0.9 ML of Pt is significantly larger than the -90 mV reported by Lima and Gonzalez [15] for a monolayer of Pt on Rh/C. In that work, it was concluded that the shift in the CO stripping potential induced by the Rh core was due primarily to electronic and geometric effects, which lowered the d-band center and decreased the CO adsorption strength. These effects are unique to the core-shell structure since CO stripping at PtRh alloy NP occurs at approximately the same potential as at Pt [15, 22].

For Pt-based NP, less electronegative metals (M), such as Ru and Sn, can provide a co-catalytic effect in which CO oxidation is promoted at lower potentials by surface M–OH groups, via a “bifunctional” mechanism. The lack of influence of alloyed Rh on CO stripping indicates

that Rh does not promote CO oxidation via the "bifunctional" mechanism, and therefore that the low stripping potentials observed here and in [15] for Rh@Pt were not due to exposed Rh.

The abrupt change in the position of CO stripping peak at ca. 2 ML in Fig. 4 is consistent with the very short range of the electronic effect [17, 20]. For CO stripping from Ru@Pt NP, it was found that distinct peaks, separated by ca. 170 mV, could be resolved for CO molecules adsorbed on the 1st and 2nd Pt monolayers [20]. The changes observed from $Rh_{72}@Pt_{28}$ to $Rh_{54}@Pt_{46}$ in Fig. 4 are similar to those reported for increasing the coverage of Pt on Ru from 1 to 2 ML [20].

In addition to decreasing the CO adsorption strength, the Rh core promotes oxidation of the Pt surface to produce the Pt-OH sites required for oxidation of the adsorbed CO. Consequently, there is a correlation between the shift with increasing Pt coverage of the CO oxidation peak in Fig. 3 with the Pt oxidation wave in Fig. 2. However, this appears to have a smaller influence than weakening of CO adsorption, since the effect on Pt oxidation is most pronounced at 1 ML, while the effect on CO oxidation is most pronounced at 2 ML.

3.4. Oxidation of Dissolved Carbon Monoxide

Voltammetric oxidation of CO in the bulk solution provides crucial information for relating CO stripping results to formic acid [21] and reformate (CO contaminated H_2) oxidation [23]. Although rarely applied for bimetallic catalysts [21], it has recently been used to investigate the role of Ru oxide in promoting CO oxidation at Pt [24].

Voltammograms at Rh/C, Rh@Pt/C, and Pt/C coated electrodes in CO-saturated H_2SO_4(aq) changed significantly with potential cycling, as reported for Pt and attributed to changes in surface structure [25]. Approximately steady state voltammograms, recorded for the 10th cycle are shown in Fig. 5. In all cases, there was little current on the forward scan until a

sharp peak at ca. 0.7 V, that was more positive than the CO stripping peak observed for the same catalyst in Fig. 4. There is no clear trend in the position of this peak and no correlation with the position of the stripping peak. For example, it is at a higher potential at Rh/C (0.72 V) than for Pt/C (0.70 V), while the CO stripping peak in Fig. 4 is lower for Rh/C.

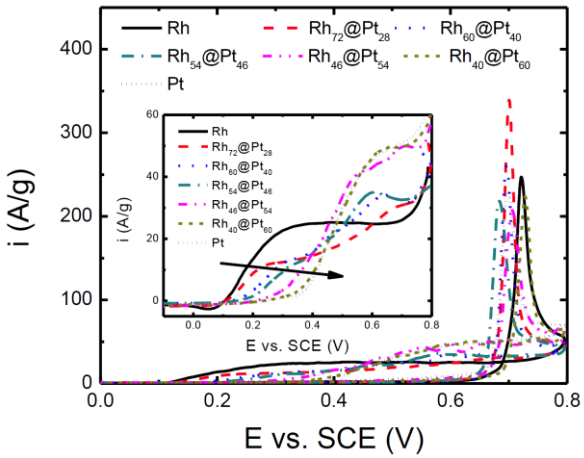

Figure 5. Cyclic voltammetry (10th cycle, 20 mV s^{-1}) of Rh/C, Rh@Pt/C, and Pt/C coated GC electrodes in CO-saturated 0.1 M H_2SO_4, with the current normalized to the total mass of Rh+Pt.

The reverse scans in Fig. 5 are similar in appearance to rotating disc voltammograms although the electrode was not rotated in these experiments. The plateaus and inflection points in the current suggest that there are regions that are controlled primarily by mass transport. Since the wave shape for Pt is very similar to that reported for a Pt electrode rotated at 100 rpm in [26], and for a stationary Pt electrode in [25], and it was demonstrated in [25] that the mass transport limit was reached at the stationary electrode, these regions are referred to here as limiting currents.

The reverse scans in Fig. 5 can best be compared by using the limiting currents and their half-wave potentials ($E_{½}$). The half-wave potentials (there were two in some cases) show a

strong correlation with the CO stripping potential. They were lowest, and similar (ca. 0.20 V), for Rh/C and $Rh_{72}@Pt_{28}$ (0.9 ML Pt), and increased as the Pt shell thickness was increased. $Rh_{40}@Pt_{60}$ (2.7 ML Pt) and Pt/C had very similar reverse scan profiles, with $E_{½} \sim 0.48$ V. Interestingly, the limiting current also show a correlation with the Pt shell thickness, with the currents for the Rh@Pt/C catalysts closer to those for Rh/C or Pt/C depending on the Rh:Pt ratio. The limiting currents for $Rh_{40}@Pt_{60}$/C and Pt/C were both ca. 50 A g^{-1} (at ca. 0.65 V), and $Rh_{46}@Pt_{54}$/C was similar, while Rh/C had a limiting current of 24 A g^{-1} from 0.35 to 0.65 V.

The sharp peaks observed in the forward scans in Fig. 5 are a consequence of the high CO coverage obtained in the presence of bulk CO, which blocks the formation of the M-OH sites required for CO stripping. It is referred to as an "ignition" peak [26]. On the reverse scan, continuous CO oxidation occurs at Pt under mass transport control and then decreases as the surface becomes covered with adsorbed CO [25, 26]. The position of the ignition peak reflects the rate of autocatalytic oxidation of CO and is determined by the competition between CO and OH adsorption [26]. The lack of correlation with the CO striping peaks in Fig. 4 indicates that the ignition peaks do not reflect the inherent CO oxidation activity. Instead, their position is controlled primarily by the structure of the catalyst surface, and the types of active sites available for –OH adsorption [25].

In contrast, the position of the half-wave potential on the reverse scan does show a strong correlation with the CO stripping potential. It is controlled by the potential of M-OH reduction and the rate and strength of CO adsorption, and therefore it provides valuable information on the influence of the Rh@Pt shell thickness on these processes. The ability of the Rh/C and lower Pt loading Rh@Pt/C catalysts to oxidize CO at much lower potentials than Pt/C, seen in Fig. 5, can be attributed primarily to the lower potential for M-OH reduction since it parallels the changes in

the M-OH reduction peak in Fig. 3. This is highly significant for the oxidation of formic acid and reformate since both of these reactions occur with partial coverage of the catalyst by CO.

The Rh/C wave on the reverse scan was clearly not purely mass transport limited since its limiting current was lower than for Pt/C. The other Rh@Pt samples show a split wave with a shoulder more characteristic of Rh/C and a higher potential feature more characteristic of Pt/C. The correlation of the shapes of these waves with the changes in the oxide reduction waves in Fig. 3 suggests that they may reflect the relative fractions of electronically Pt-OH like and Rh-OH like sites. This effect may provide a method for determining the relative amounts of Rh-OH, Rh-Pt-OH, and Rh-Pt-Pt-OH layers at the catalyst surface [20].

3.5. Formic Acid Oxidation

Fig. 6 shows cyclic voltammograms, normalized on a Rh + Pt mass basis, for formic acid oxidation at the Rh/C, Rh@Pt/C, and Pt/C catalysts. Relative to Pt/C, the presence of a Rh core increased the currents at all potentials on the forward scan, and in most cases increased the currents on the reverse scan. In comparison, the currents for formic acid oxidation at Rh/C were very low, except for a peak at 0.05 V when the Rh-OH layer was reduced on the reverse scan.

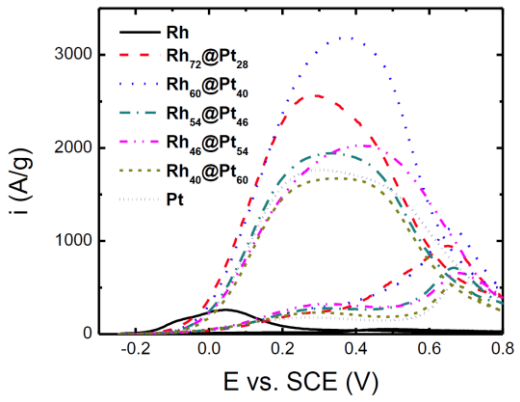

Figure 6. Cyclic voltammetry (20 mV s^{-1}) of Rh/C, Rh@Pt/C, and Pt/C coated GC electrodes in 0.1 M H_2SO_4 + 1 M formic acid, with the current normalized to the total mass of Rh+Pt.

For the Pt/C electrode, the first peak on the forward scan (at 0.25 V) is due to the dehydrogenation pathway for direct oxidation of formic acid to CO_2 (direct pathway), while the peak at 0.70 V is due to the oxidation of CO_{ads} formed by dehydration of formic acid (indirect pathway). The Rh core caused different effects on these two pathways depending on the thickness of the shell. For the thickest Pt shell (2.7 ML for $Rh_{40}@Pt_{60}$) the current for the direct pathway was increased slightly relative to Pt/C, but the indirect pathway was not significantly affected. The thinnest Pt shell (0.9 ML for $Rh_{72}@Pt_{28}$) also increased the current for the direct pathway slightly, but approximately doubled the current for the indirect pathway, and produced a notable low potential shoulder over the 0.4-0.6 V region. Consequently, the current for formic acid oxidation was much higher for $Rh_{72}@Pt_{28}$ over this potential range than for Pt/C. Increasing the Pt coverage to 1.4 ML ($Rh_{60}@Pt_{40}$) did not influence this region significantly, but did increase the current for the direct pathway. The highest current for the direct pathway was obtained at 2.3 ML ($Rh_{46}@Pt_{54}$), close to the value of 2.6 ML reported in [13].

The effects of the Pt shell thickness can largely be explained by the electronic and geometric effects of the Rh core on the strength of CO bonding to the Pt surface. These effects are strongest for the $Rh_{72}@Pt_{28}$/C catalyst, and decrease as the Rh:Pt ratio is decreased (Fig. 4). The weaker CO bonding, combined with the earlier onset of Pt-OH formation (Fig. 2), increases the rate of the indirect oxidation of formic acid and allows it to occur at lower potentials. This effect, over the 0.4 to 0.7 V potential range, is most pronounced at low Pt shell thicknesses.

With thicker Pt shells, the electronic effect becomes less significant than the lattice compression effect [17], and the influence of the Rh core on CO stripping becomes insignificant. This indicates that the influence on CO stripping is primarily an electronic effect. In contrast, the effect of the Rh core on the direct pathway initially increases with increasing shell thickness, and

is more persistent, suggesting that it is due to compression of the Pt lattice. The peak in the rate of the direct pathway at 2.3 ML is presumably due to an optimum balance between the electronic and geometric effects. Both of these effects lower of the d-band center and weaken the bonding of both CO and formic acid [27]. However, if formic acid adsorption is too weak, the effect of the weaker CO adsorption will be diminished.

The reverse (cathodic) scans for formic acid oxidation in Fig. 6 reflect the relative rates of Pt-OH reduction, which causes the initial increase in anodic current from 0.8 to ca. 0. 4 V, and the accumulation of CO_{ads}, which contributes to the decreasing current after the peak [28]. The high peak currents are primarily due to the direct pathway at the clean Pt surface exposed by reduction of the Pt-OH layer. The superiority of the Rh@Pt/C catalysts on the reverse scan largely reflects the weaker CO bond strength, although the effects of the Rh core on formic acid adsorption and Pt-OH reduction will also play a role. Unraveling these factors from the time and potential dependence is too complex to allow any clear conclusions to be drawn from the cathodic scans.

Chronoamperometric oxidation of formic acid was investigated over a range of potentials. Prior to each potential step, the potential of the electrode was stepped to 0.6 V for 15 s to remove adsorbed species (primarily CO) and produce a clean catalyst surface. Fig. 7A shows data recorded at 0.3 V for all of the catalysts, while Fig. 7 B summarizes the data at all potentials as plots of the current recorded at 240 s vs. potential. Although the data at 0.3 V in Fig. 7A corresponds to the voltammetric peak (forward scan) for the direct pathway, they do not show the same trend with changing composition of the Rh@Pt catalysts, and the currents are much greater. This is due primarily to the removal of CO_{ads} prior to each potential step, and formation

of an activated Pt surface by reduction of Pt-OH. Consequently, the currents were much higher during chronoamperometry at 0.3 V than for the forward voltammetric peak at ca. 0.3 V.

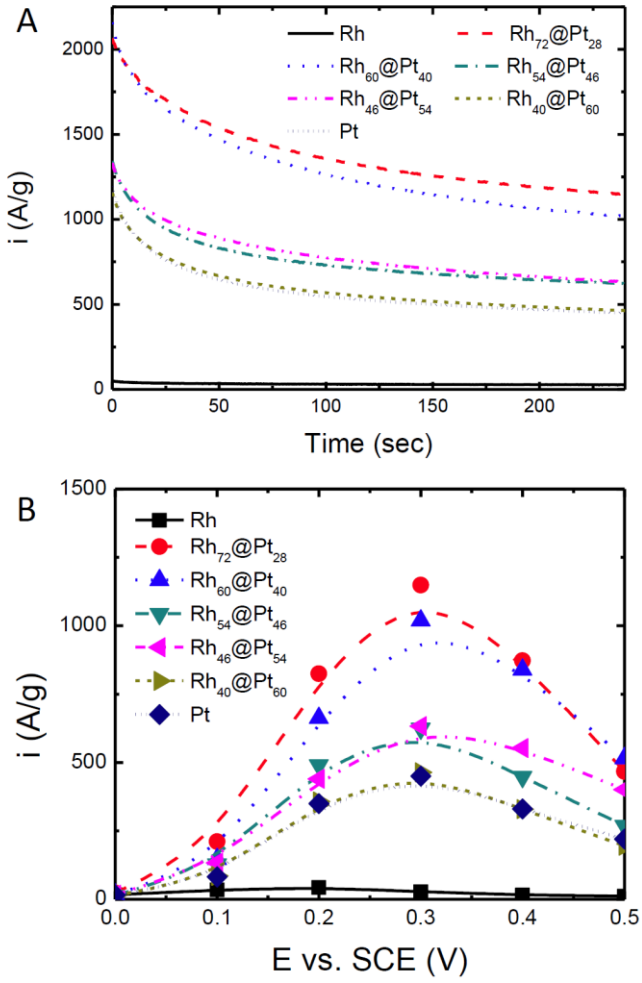

Figure 7. A. Chronoamperometry at 0.3 V for at Rh/C, Rh@Pt/C, and Pt/C coated GC electrodes in 0.1 M H_2SO_4 + 1 M formic acid, with the current normalized to the total mass of Rh+Pt. **B.** Currents at 240 s for chronoamperometry at various potentials.

The initial currents in Fig. 7A provide the rate of formic acid oxidation the activated Pt surface, while the rate of decay indicates the rate of CO_{ads} accumulation. The decay rates were similar for Pt/C and the Rh@Pt/C catalysts, indicating that the differences were primarily in the

intrinsic activity of the clean surfaces. The $Rh_{72}@Pt_{28}/C$ and $Rh_{60}@Pt_{40}/C$ catalysts provided the highest activity, with poisoning by CO_{ads} slightly faster for $Rh_{60}@Pt_{40}/C$. Increasing the shell thickness to ca. 2 ML ($Rh_{54}@Pt_{46}/C$ and $Rh_{46}@Pt_{54}/C$) decreased the current by a factor of ca. 2, indicating that the stronger electronic effect of Rh on the 1st Pt layer was the key factor responsible for the enhanced activity of the Rh@Pt/C catalysts over Pt/C. This is supported by the observation that the activity for the $Rh_{40}@Pt_{60}/C$ catalyst (2.7 ML) was almost the same as for Pt/C.

The data at other potentials (Fig. 7B) show a similar pattern, with a large drop in activity as the 1st Pt layer is covered with a 2nd layer. Interestingly, the abruptness of the change was less pronounced at 0.5 V, suggesting that lattice compression may play a role in enhancing the rate of the indirect pathway. However, once the 2nd layer was completely covered, the activity at all potentials was indistinguishable from that of Pt/C.

4. Conclusions

Varying the Pt coverage of Rh@Pt NP has provided insight into the effects of electronic changes and lattice compression on CO and formic acid oxidation. The presence of the Rh core shifts the onset of Pt-OH formation to lower potentials, which facilitates CO oxidation at lower potentials. In combination with weakening of the Pt-CO bond by lowering the Pt d-band center, this shifts the peak potential for CO stripping below the value for Rh alone. These effects diminish rapidly with increasing shell thickness, indicating that they are primarily electronic in nature. Oxidation of bulk CO, which can persist on the reverse scan until ca. 0.1 V vs. SCE when there is a single monolayer of Pt, provides complementary information on the role of Pt-OH. This is an important factor in the enhancement of formic acid oxidation rates at Rh@Pt NP, where ca. 1 ML of Pt provides the highest activity for the direct pathway in chronoamperometry,

and the cathodic scan in voltammetry. In contrast, the peak for the direct pathway was highest for ca. 2 ML of Pt on the anodic scan, implying that compression of the Pt lattice also plays a significant role.

Acknowledgment

This work was supported by the Natural Sciences and Engineering Research Council of Canada and Memorial University.

References

[1] M. Oezaslan, F. Hasche, P. Strasser, Pt-based core-shell catalyst architectures for oxygen fuel cell electrodes, J. Phys. Chem. Lett., 4 (2013).

[2] M.B. Gawande, A. Goswami, T. Asefa, H.Z. Guo, A.V. Biradar, D.L. Peng, R. Zboril, R.S. Varma, Core-shell nanoparticles: synthesis and applications in catalysis and electrocatalysis, Chem. Soc. Rev., 44 (2015) 7540-7590.

[3] R.Y. Jiang, S.O. Tung, Z. Tang, L. Li, L. Ding, X.G. Xi, Y.Y. Liu, L. Zhang, J.J. Zhang, A review of core-shell nanostructured electrocatalysts for oxygen reduction reaction, Energy Storage Mater., 12 (2018) 260-276.

[4] R.M. Anderson, D.F. Yancey, L. Zhang, S.T. Chill, G. Henkelman, R.M. Crooks, A Theoretical and Experimental Approach for Correlating Nanoparticle Structure and Electrocatalytic Activity, Acc. Chem. Res., 48 (2015) 1351-1357.

[5] M.T. Gorzkowski, A. Lewera, Probing the limits of d-band center theory: Electronic and electrocatalytic properties of Pd-shell-Pt-core nanoparticles, J. Phys. Chem. C, 119 (2015) 18389-18395.

[6] A. Kongkanand, N.P. Subramanian, Y.C. Yu, Z.Y. Liu, H. Igarashi, D.A. Muller, Achieving high-power PEM fuel cell performance with an ultralow-Pt-content core-shell catalyst, ACS Catalysis, 6 (2016) 1578-1583.

[7] L. Zhang, S.N. Yu, J.J. Zhang, J.L. Gong, Porous single-crystalline AuPt@Pt bimetallic nanocrystals with high mass electrocatalytic activities, Chemical Science, 7 (2016) 3500-3505.

[8] H.Y. Liu, Y.J. Song, S.S. Li, J. Li, Y. Liu, Y.B. Jiang, X.W. Guo, Synthesis of core/shell structured Pd_3Au@Pt/C with enhanced electrocatalytic activity by regioselective atomic layer deposition combined with a wet chemical method, RSC Advances, 6 (2016) 66712-66720.

[9] T.-Y. Chen, T.-L. Lin, T.-J.M. Luo, Y. Choi, J.-F. Lee, Effects of Pt shell thicknesses on the atomic structure of Ru-Pt core-shell nanoparticles for methanol electrooxidation applications, Chemphyschem, 11 (2010) 2383-2392.

[10] E.N. El Sawy, H.A. El-Sayed, V.I. Birss, Clarifying the role of Ru in methanol oxidation at Ru_{core}@Pt_{shell} nanoparticles, Phys. Chem. Chem. Phys., 17 (2015) 27509-27519.

[11] S. Alayoglu, A.U. Nilekar, M. Mavrikakis, B. Eichhorn, Ru-Pt core-shell nanoparticles for preferential oxidation of carbon monoxide in hydrogen, Nature Materials, 7 (2008) 333-338.

[12] S. Goto, S. Hosoi, R. Arai, S. Tanaka, M. Umeda, M. Yoshimoto, Y. Kudo, Particle-size- and Ru-core-induced surface electronic states of Ru-core/Pt-shell electrocatalyst nanoparticles, J. Phys. Chem. C, 118 (2014) 2634-2640.

[13] E.W. Harak, K.M. Koczkur, D.W. Harak, P. Patton, S.E. Skrabalak, Designing efficient catalysts through bimetallic architecture: Rh@Pt nanocubes as a case study, Chemnanomat, 3 (2017) 815-821.

[14] L. Fang, J.L. He, S. Saipanya, X.P. Huang, Preparation of Rh-5@Pt-x/C core-shell nanoparticles for electrocatalytic oxidation of ethanol, Int. J. Electrochem. Sci., 10 (2015) 5350-5357.

[15] F.H.B. Lima, E.R. Gonzalez, Electrocatalysis of ethanol oxidation on Pt monolayers deposited on carbon-supported Ru and Rh nanoparticles, Appl. Catal. B Environ, 79 (2008) 341.

[16] S. Alayoglu, B. Eichhorn, Rh-Pt bimetallic catalysts: Synthesis, characterization, and catalysis of core-shell, alloy, and monometallic nanoparticles, J. Am. Chem. Soc., 130 (2008) 17479-17486.

[17] A. Schlapka, M. Lischka, A. Gross, U. Kasberger, P. Jakob, Surface strain versus substrate interaction in heteroepitaxial metal layers: Pt on Ru(0001), Phys. Rev. Lett., 91 (2003) 016101.

[18] P. Strasser, S. Koh, T. Anniyev, J. Greeley, K. More, C.F. Yu, Z.C. Liu, S. Kaya, D. Nordlund, H. Ogasawara, M.F. Toney, A. Nilsson, Lattice-strain control of the activity in dealloyed core-shell fuel cell catalysts, Nature Chemistry, 2 (2010) 454-460.

[19] P. Ochal, J.L.G. de la Fuente, M. Tsypkin, F. Seland, S. Sunde, N. Muthuswamy, M. Ronning, D. Chen, S. Garcia, S. Alayoglu, B. Eichhorn, CO stripping as an electrochemical tool for characterization of Ru@Pt core-shell catalysts, J. Electroanal. Chem., 655 (2011) 140-146.

[20] E.N. El Sawy, H.A. El-Sayed, V.I. Birss, Novel electrochemical fingerprinting methods for the precise determination of Pt-shell coverage on Ru-core nanoparticles, Chem. Commun., 50 (2014) 11558-11561.

[21] E.N. El Sawy, P.G. Pickup, Formic acid oxidation at Ru@Pt core-shell nanoparticles, Electrocatalysis, 7 (2016) 477-485.

[22] K. Bergamaski, E.R. Gonzalez, F.C. Nart, Ethanol oxidation on carbon supported platinum-rhodium bimetallic catalysts, Electrochim. Acta, 53 (2008) 4396-4406.

[23] S. Kirsch, R. Hanke-Rauschenbach, A. El-Sibai, D. Flockerzi, K. Krischer, K. Sundmacher, The S-shaped negative differential resistance during the electrooxidation of H_2/CO in polymer electrolyte membrane fuel cells: Modeling and experimental proof, J. Phys. Chem. C, 115 (2011) 25315-25329.

[24] P.Y. Olu, T. Ohnishi, D. Mochizuki, W. Sugimoto, Uncovering the real active sites of ruthenium oxide for the carbon monoxide electro-oxidation reaction on platinum: The catalyst acts as a co-catalyst, J. Electroanal. Chem., 810 (2018) 109-118.

[25] A.V. Rudnev, A. Kuzume, Y.C. Fu, T. Wandlowski, CO oxidation on Pt(100): New insights based on combined voltammetric, microscopic and spectroscopic experiments, Electrochim. Acta, 133 (2014) 132-145.

[26] M.T.M. Koper, T.J. Schmidt, N.M. Markovic, P.N. Ross, Potential oscillations and S-shaped polarization curve in the continuous electro-oxidation of CO on platinum single-crystal electrodes, J. Phys. Chem. B, 105 (2001) 8381-8386.

[27] M.A. Rigsby, W.P. Zhou, A. Lewera, H.T. Duong, P.S. Bagus, W. Jaegermann, R. Hunger, A. Wieckowski, Experiment and theory of fuel cell catalysis: Methanol and formic acid decomposition on nanoparticle Pt/Ru, J. Phys. Chem. C, 112 (2008) 15595-15601.

[28] Y.Z. Zhao, X.M. Li, J.M. Schechter, Y.A. Yang, Revisiting the oxidation peak in the cathodic scan of the cyclic voltammogram of alcohol oxidation on noble metal electrodes, RSC Advances, 6 (2016) 5384-5390.